methane

MDPI

Article

Morphology-Controlled WO_3 for the Photocatalytic Oxidation of Methane to Methanol in Mild Conditions

Dumindu Premachandra [1,2] and Michael D. Heagy [2,*]

[1] Department of Chemistry, New Mexico Institute of Mining and Technology 801, Leroy Pl, Socorro, NM 87801, USA
[2] School of Chemistry and Materials Science, Rochester Institute of Technology, One Lomb Memorial Drive, Rochester, NY 14623, USA
* Correspondence: mdhsch@rit.edu

Abstract: Since WO_3 is a relatively abundant metal oxide and features the ability to absorb in the visible spectrum, this non-toxic semiconductor is a promising photocatalyst among sustainable materials. These properties have delivered intriguing catalytic results in the conversion of methane to methanol; however, initial investigations indicate low photocatalytic efficiency resulting from fast recombination of photogenerated charges. To explore this aspect of inefficiency, five different morphologies of WO_3 consisting of micron, nanopowder, rods, wires, and flowers were obtained and characterized. In addition, several electron capture agents/oxidizers were investigated as a means of improving the separation of photogenerated charges. The photocatalytic activity of different morphologies was assessed via CH_3OH formation rates. Based on our results, WO_3 flowers produced the highest methanol productivity (38.17 ± 3.24 μmol/g-h) when 2 mM H_2O_2 was present, which is approximately four times higher in the absence of H_2O_2. This higher methanol production has been attributed to the unique structure-related properties of the flower-like structure. Photoluminescence emission spectra and diffuse reflectance data reveal that flower structures are highly catalytic due to their reduced electron/hole recombination and multiple light reflections via petal-like hollow chambers.

Keywords: Methane oxidation; photochemical; methanol; hierarchical nanostructures; nanoflowers

Citation: Premachandra, D.; Heagy, M.D. Morphology-Controlled WO_3 for the Photocatalytic Oxidation of Methane to Methanol in Mild Conditions. *Methane* **2023**, *2*, 103–112. https://doi.org/10.3390/methane2010008

Academic Editor: Patrick Da Costa

Received: 12 January 2023
Revised: 9 February 2023
Accepted: 15 February 2023
Published: 17 February 2023

1. Introduction

Methane (CH_4) is the simplest carbon-rich organic compound that is abundant in nature, and it is a clean, safe, and potentially alternative energy source to petroleum [1]. Currently, methane is extensively used to generate electricity and heat, and as a raw material in chemical production, as well as for transportation [2,3] and its usage is expected to grow by roughly 50% from 2018 to 2050, based on the United States Energy Information Administration [4]. In addition to the high cost of transporting gaseous methane via pipelines, leaks and transmission failures are inevitable. Given methane's ranking as the second-leading greenhouse gas, excessive emissions of natural gas threaten the environment. To utilize methane to its fullest energy extent, address methane leaks, and mitigate climate forcing, environmentally benign capture and conversion techniques for natural gas are being sought toward value-added products such as methanol [5–7], olefins [8], and hydrogen [9]. Although methanol has half the energy density compared to gasoline or diesel, it has a high research octane number (RON of 133) and blends well with conventional liquid fuels [10]. Since current thermo-catalytic conversions of methane to methanol require high temperatures (400–500 °C) as well as high pressure (50 atm), they are less economically feasible [2,11]. Because of the highly energetic C-H bond and the propensity of methane overoxidation to CO or CO_2, semiconductor development toward selective photocatalytic oxidation under mild aqueous conditions to methanol has been recently dubbed a "dream reaction" [12,13].

Light-driven methane oxidation to methanol has been the subject of several studies over the past decade. One of the more promising materials among semiconductor photocatalysts, tungsten trioxide (WO_3) has emerged as a viable contender [3,14–17]. The lower bandgap energy of this material (2.4–2.8 eV) makes it an active photocatalyst for visible light; it has high chemical stability, is nontoxic, and can oxidize moderately [15]. WO_3 semiconductors are energetically advantageous for oxidizing water to form hydroxyl radicals ($OH^{\bullet}$) due to its deep valance band edge ($E_{VB} \approx +3.1$ V vs. NHE at pH 0). In addition, it possesses a positive conduction band edge ($E_{CB} \approx +0.4$ V vs. NHE at pH 0) which is insufficient to reduce dissolved oxygen ($O_2/O_2^{\bullet}$); thus, unwanted side reactions such as the overoxidation of methanol (via $O_2^{\bullet}$) can be avoided. A pioneering experiment conducted by Gondal et al., demonstrated that WO_3 is more effective than TiO_2 and NiO for methanol production [14]. Prior studies have investigated different photocatalytic systems based on WO_3 to enhance selectivity and methanol production, such as metal doping [16,17], mesoporous WO_3 structures [15,16], and loading co-catalysts [3]. In contrast, chemical additives such as H_2O_2 [3,15,18,19] (oxidant) and electron capture agents (ex. Fe^{3+}, methyl viologen dichloride hydrate (MV^{2+})) [15,20] were reported to enhance the photogenerated charge separation.

According to several studies, photocatalysis is strongly influenced by the morphology of nanomaterials [21–24]. In addition to the specific surface area, morphology is also closely related to adsorption–desorption during catalysis [25]. In nanostructures, the coordination number of the atoms determines the number of surface-active sites. In nanosheet and nanorods, for example, atoms near the corners and edges have more adsorption active sites than bulk atoms within nanospheres due to their lower coordination number [25,26]. Additionally, it has been reported that WO_3 with flower-like and wheel-like structures (hierarchical structures) offered greater photogenerated charge separation efficiency and a lower rate of recombination, resulting in greater photocatalytic activity for degradation of rhodamine B (RhB) [27]. Therefore by controlling the morphology of the nanoparticle, the efficiency of photocatalytic reaction can be elevated by increasing the number of catalytic sites and the efficiency of photoinduced charge separation [28,29]. The morphology of a nanoparticle can be optimized via different dimensions such as 0D, 1D, 2D, and 3D. Over the past few years, a number of methods have emerged to synthesize different morphologies of WO_3 nanomaterials to utilize in various applications such as nano-quantum dots (0D; formaldehyde gas sensing) [30], nanorods (1D; degradation of organic pollutants) [31], nanoplates (2D; gaseous acetaldehyde degradation) [32], flowers (3D; photo-oxidation of m-xylene) [33], etc. Tungsten trioxide 3D hierarchical architectures are generally composed by assemblies of nanorods, nanosheets, or nanoplates to form highly ordered nano or microstructures [28]. Thus, they feature unique morphologies with high porosity and high surface area. It has been reported that these WO_3 hierarchical architectures possess superior gas-sensing performance, such as for ethanol [34,35]. The unique structure-related properties of 3D hierarchical structures motivated us to design a set of experiments to evaluate their photocatalytic activity in the context of several morphologies. To the best of our knowledge, no morphology-controlled study of methane partial-oxidation to methanol using WO_3 has been reported.

2. Results and Discussion

Surfaces of semiconductor materials with different architectural designs can have different photocatalytic efficiencies. This comparative study investigated five different architectures that were either convenient to synthesize or commercially available. FESEM was used to compare the particle sizes of the nanoarchitectures (Figure 1a–e) and the particle sizes ranged from 100 nm to 20 µm. Based on the PXRD (Supplementary Materials; Figure S1), these materials belong to three different crystal phases: monoclinic, hexagonal, and orthorhombic. It appears that the XRD peak on 14° of hexagonal-WO_3 wires [(100)] was split into two, indicating that the wires are not entirely hexagonal. The additional peak may be the result of a slight change in the crystal system from hexagonal to orthorhombic [36].

The bandgaps of the morphologies vary from 2.4–2.8 eV, which were obtained by treating the DRS spectra (Figure 2a) to obtain a Kubelka–Munk plot using the following equation.

$$(\alpha h\upsilon)^n = B\left(h\upsilon - E_g\right) \quad (1)$$

where α is the absorption coefficient, $h\upsilon$ equates to the photon energy, B is a constant, Eg is the bandgap, and n refers to the nature of the photoelectron transition (n = 2 for direct transition, n = $\frac{1}{2}$ for indirect transition). WO_3 is a well-known indirect type bandgap semiconductor [37,38], therefore $[A(h\nu)^{1/2}]$ against $h\nu$ (where A= absorbance) was plotted (Figure 2b). Using the linear fit, the bandgap energy can be obtained by intersecting the $h\nu$ axis with the steepest region of the Kubelka–Munk spectrum as shown in Figure 2b. When compared to other architectures, the DRS spectrum for WO_3 flowers showed significantly higher absorption. This may be due to the multiple reflections of incident light between the interconnected nanosheets and the hollow spheres in the middle, enhancing the harvesting of light [39]. BET surface area measurements were used to gain information on the surface area of all the architectures. Micron and nanopowders of WO_3 materials showed low surface area (below 10 m^2/g) while the rest of the materials displayed higher surface area (above 15 m^2/g). The highest surface area was obtained for the WO_3 rods, ~ 20 m^2/g. All the characterization data are listed in Table 1.

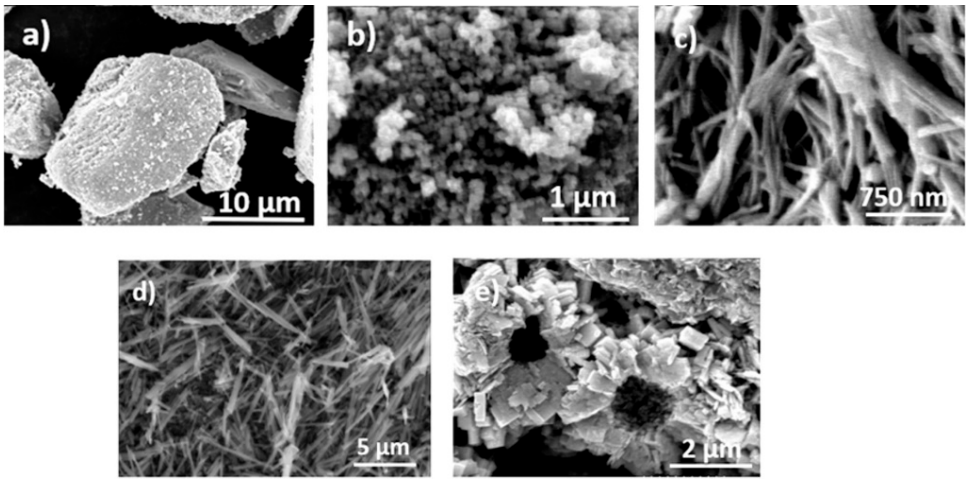

Figure 1. FESEM images of (**a**) WO_3 micron, (**b**) WO_3 nanopowder, (**c**) WO_3 wires, (**d**) WO_3 rods, and (**e**) WO_3 flowers.

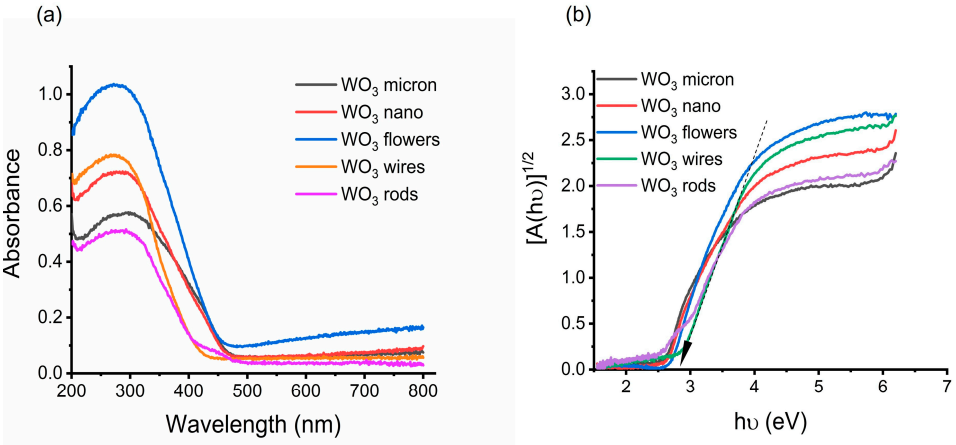

Figure 2. (**a**) Diffuse reflectance spectra of WO_3 particles (**b**) Kubelka–Munk-treated plots of WO_3 particles.

Table 1. Characteristics of different WO_3 materials and methanol productivity.

WO_3 Architecture	Crystal Modification	Bandgap (eV)	BET Surface Area (m^2/g)
micron	monoclinic	2.48 ± 0.06	4.3
nanopowder	monoclinic	2.58 ± 0.05	7.1
rods	hexagonal	2.71 ± 0.08	19.6
wires	hexagonal	2.75 ± 0.05	17.0
flowers	orthorhombic	2.59 ± 0.09	16.9

WO_3 nanostructures were further characterized using X-ray photoelectron spectroscopy (XPS) survey spectra. The total XPS spectrum also shows the presence of tungsten and oxygen elements in all WO_3 nanostructures. Rods, wires, and flowers displayed additional Na 1s (7.83%, 8.18%, and 7.75%, respectively), which resulted from precursors. In all WO_3 structures, the W 4f spectra and fit curves are consistent with well-oxidized W atoms as shown in Figure 3a. Peaks at ~37.8 eV and ~35.9 eV correspond to the binding energies of W $4f_{7/2}$ and W $4f_{5/2}$, respectively [32,40,41]. These energy values are consistent with W^{6+} peaks based on the binding energy values that were previously reported. Figure 3b illustrates the XPS spectrum of O 1s for the prepared samples at approximately 530.5 eV caused by oxygen atoms in the lattice. Moreover, the second peak around 531.5 eV (obtained by curve fitting) can be attributed to a surface-adsorbed oxygen group or a hydroxyl group [40,42]. W 4f and O 1s were similar in all the samples, indicating that all WO_3 have similar surface compositions.

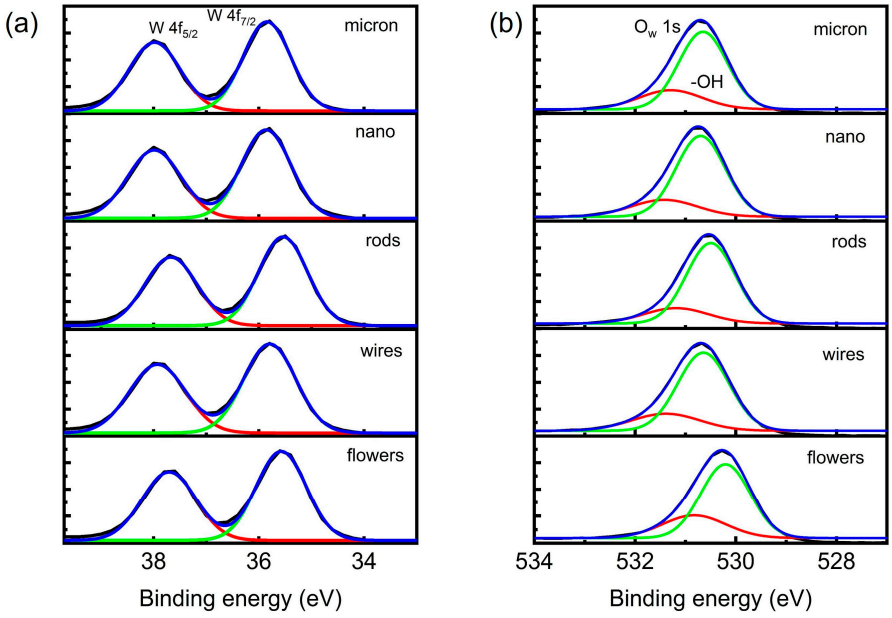

Figure 3. XPS spectra of (**a**) W 4f and (**b**) O 1s for all the WO_3 structures.

Photocatalysis offers a unique pathway to promote difficult reactions under ambient temperatures. Figure 4 presents a schematic of the proposed mechanism involving different pathways of methane activation toward the formation of methanol. In a study by Villa et al., fluorine was incorporated into the surface of WO_3 to minimize catalyst–reactant interaction, which revealed that free OH• can produce methyl radicals by initiating the reaction with methane, while surface-bound OH• played a major role in the oxidation of methane radicals to methanol in addition to methane activation [43]. As an initial experiment for selecting the reaction conditions and selecting an electronic scavenger (or oxidant) for the partial oxidation of methane to methanol, WO_3 flowers were used. Several experiments were

conducted to determine which conditions and chemical additives, such as H_2O_2, Fe^{3+}, and N_2H_4, produced the most methanol, and based on these results, the remaining experiments were conducted. The Fe^{3+} and H_2O_2 have been tested before in previous studies where Fe^{3+} was used as an electron capture agent to prevent production of O_2^- which then led to the production of CO_2 by over oxidation of CH_3OH [15,19]. N_2H_4 is also a potential candidate as an electron scavenger that has not been previously tested. $N_2H_4/2\ NH_3$ is +0.7 V at pH = 7 and has a comparatively positive reduction potential to the conduction band of WO_3. However, due to the poor methanol productivity, both Fe^{3+} and N_2H4 have been ruled out from further experimentation (Supplementary Materials; Figure S2). According to the initial data shown, the combination of WO_3 flowers and 2 mM H_2O_2 yields the highest catalytic activity towards the formation of methanol. A significant improvement was observed in methanol production when WO_3 flowers/2 mM H_2O_2 were compared to bare WO_3 flowers (approximately four times higher). However, when the H_2O_2 concentration was doubled, the methanol yield decreased. The promotional effect of H_2O_2 is twofold; it improves the methanol formation by the generation of more OH• in the medium, and when there is an excess of OH• (from H_2O_2), it causes over-oxidation of methanol to suppress the methanol yield. Neither the blank nor the dark experiment produced any methanol. The reaction temperature was maintained at ~ 50 °C to increase the methanol concentration of the headspace rather than in the solution.

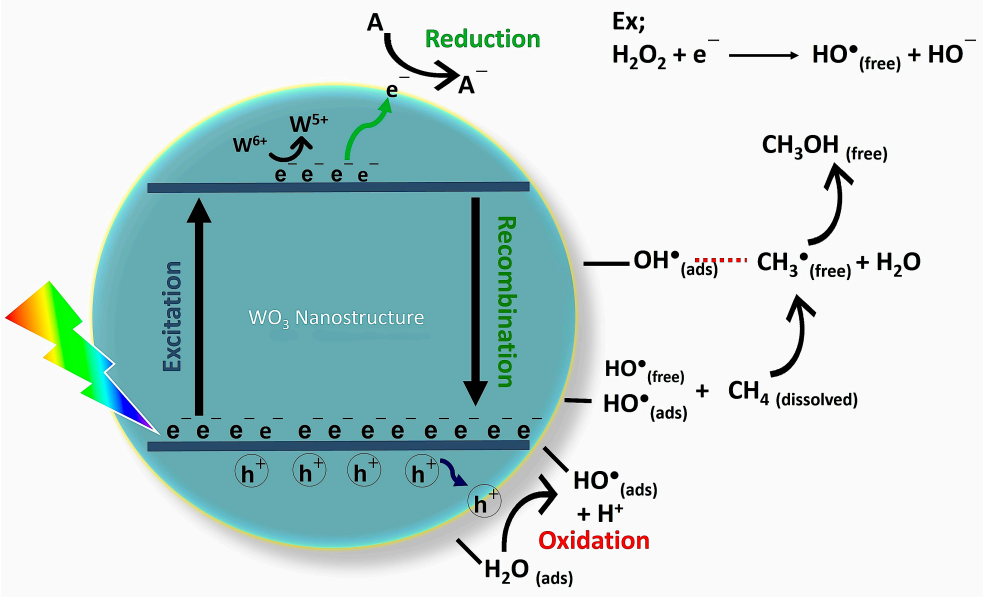

Figure 4. Schematic of the proposed mechanism of photocatalytic methane partial oxidation to methanol.

All reactions involving morphologies in the presence of 2 mM H_2O_2 followed a general trend in which methanol formation is high during the first 75 min, then decreases over time, and by the end of two hours, methanol formation is negligible (Supplementary Materials; Figure S3; as the triplicate measurements were associated with large errors during 0–75 min for the yield of methanol, the plot includes the yield of methanol after 75 min). This result could be due to the over-oxidation of methanol by either photogenerated holes or hydroxyl radicals in the reaction medium, which has been observed in previous studies as well [14,15,17].

To determine how efficiently charge carriers are separated, the photoluminescence (PL) emission spectra of all WO_3 structures were obtained. Figure 5a displays the corresponding spectra, revealing that the WO_3 flowers show reduced PL intensity in comparison with other structures. Electrons and holes are recombined less readily in WO_3 flowers, which indicates a reduced recombination rate. A representative WO_3 morphology producing methanol after 75 min, whose production rates were consistent across triplicates, is shown in Figure 5b.

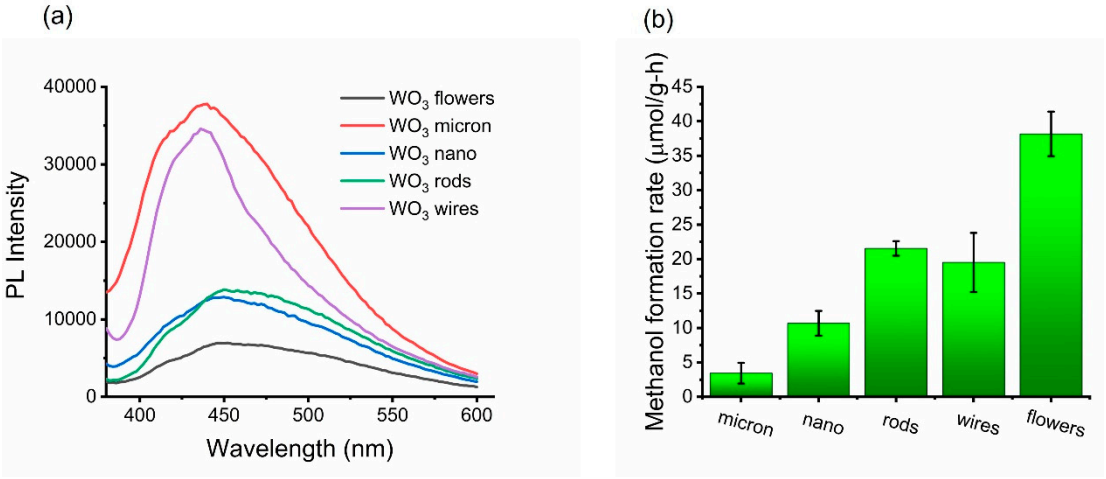

Figure 5. (**a**) Photoluminescence emission spectra of WO_3 particles (**b**) Methanol formation rate for morphology/2 mM H_2O_2 (reaction conditions: temperature of 50 °C, pH~7, UV light irradiation, CH_4/N_2 bubbling with 100 mL/min).

The highest photocatalytic rate of formation of methanol (38.17 ± 3.24 μmol/g-h) was displayed by WO_3 flowers. Both the higher productivity rate and methanol selectivity are ascribed to the following: (i) The 3D hierarchical structure, where slow recombination of photogenerated carriers on the surface may effectively contribute to the methane partial oxidation. (ii) Relatively low bandgap energy (~2.6 eV) extends the visible light absorption. (iii) Relatively high surface area (17 m^2/g) allows more surface-bound hydroxyl radical generation and hence the higher selectivity. (iv) Multiple reflections of light caused by nanosheet-like (petal) structures, as well as hollow chambers, may increase the formation of photogenerated electron/hole pairs because light interacts more with the surface of the material. In experiments involving rods and wires the methanol displayed similar productivities (21.55 ± 1.06 μmol/g-h and 19.52 ± 4.29 μmol/g-h, respectively); this may be due to the comparable bandgap energy and surface area of the two morphologies. PL emission spectra, however, suggests wires have high recombination rates, possibly due to their powdered form's high particle agglomeration, which can be seen in SEM images as well (Supplementary Materials; Figure S4). Micron and nanopowder of WO_3 have relatively low productivity rates, due mostly to the comparatively small surface areas of these two structures. Micron particles have the fastest electron/hole recombination rates among all the WO_3 structures.

The present study gives an insight into the effects of morphology control over surface area of WO_3 in the photocatalytic partial oxidation of methane to methanol as compared to previous literature involving WO_3. Many research works consider mesoporous WO_3 to be effective for methanol production because of the high surface area [3,15,16,43]. In 2015, Villa et al. [15] explored the partial oxidation of methane to methanol using mesoporous WO_3 (m-WO_3; surface area 151 m^2/g) with different chemical additives such as Fe^{3+}, Ag^+, Cu^{2+}, and H_2O_2. They reported maximum methanol productivity (55.5 μmol/g-h) for Fe^{3+}/m-WO_3 while H_2O_2/m-WO_3 was 22.6 μmol/g-h (mostly similar experimental conditions to the current study). Even though m-WO_3 has a ten times higher surface area compared to the WO_3 flowers there is no significant improvement in the rate of methanol formation. In this study, however, since materials with lower surface areas were considered, data support the suggestion that surface area influences the results when WO_3 nanopowder is compared with WO_3 rods. There is a two-fold increase in the rate of methanol formation, despite similar recombination rates. This can be explained by the OH• bound to the surface of WO_3 rods leading to higher methanol productivity. Concisely, when comparing our results with those of Villa et al., we can conclude that surface area might play a role to a certain point, then morphology control (especially hierarchical architectures) might be more

effective in the partial oxidation of methane to methanol since the incident light absorbance can be improved and electron/hole recombination rate lowered.

3. Experimental

3.1. Chemicals and Materials

$Na_2WO_4 \bullet 2H_2O$, HCl, NaCl, ethylene glycol, and WO_3 micron (<20 μm), WO_3 nanopowder (<100 nm), and WO_3 wires (diam. × L ~50 nm × 10 μm) were purchased from Sigma Aldrich and used without further purification.

3.2. Synthesis of WO_3 Rods

WO_3 rods were hydrothermally synthesized using a method adapted from Wang et al. (2008) [44]. In summary, $Na_2WO_4 \bullet 2H_2O$ (0.825 g) and NaCl (0.290 g) were dissolved in 19.0 mL deionized water, and the pH of the mixture was adjusted to 2.0 by adding 3.0 M HCl. Next, the mixture was transferred into a Teflon-lined autoclave and the hydrothermal reaction was carried out at 180 °C for 24 h. Finally, after the autoclave reached room temperature, the nanorods were collected using a centrifuge and washed with deionized water several times.

3.3. Synthesis of WO_3 Flowers

The synthesis of WO_3 flowers was adapted from Huang et al., (2012) [39]. First, $Na_2WO_4 \bullet 2H_2O$ was dissolved in ethylene glycol–water (volume ratio 1:2.5) mixture under vigorous stirring at 75 °C. Then, 12.0 M HCl was added dropwise until a yellow-like precipitate formed and next the solution was kept at 75 °C for 12 h. After that, the precipitate was collected by filtration and washed with ethanol and water and air-dried for 10 h at 60 °C. Lastly, the precipitate was calcined at 450 °C for 2 h in a furnace.

3.4. Photocatalytic Semiconductor Characterization

A UV-Vis spectrophotometer, Varian Cary 50 Scan, was used to measure UV-VIS spectra of the particles, which ranged from 800 to 200 nm in wavelength. An X'Pert Pro X-ray diffraction (XRD) instrument was used to obtain powder X-ray diffraction (PXRD). The BET surface area measurements were performed on an Autosorb-1 Quantachrome Surface Area and Porosity Analyzer. The field emission scanning electron microscope Hitachi S-4100 was used to obtain the SEM images. Diffuse reflectance spectroscopy (DRS) was performed on finely powdered WO_3 particles using a Thermo Scientific Evolution 260 Bio UV-VIS spectrophotometer with an integrated sphere. To obtain the bandgap values of semiconductor particles, the absorbance spectra were treated with a Kubelka–Munk function. To determine the sample's surface composition, an X-ray photoelectron spectroscopy (XPS) measurement was conducted on a Physical Electronics Versaprobe II XPS. The binding energies of the C 1 s peak at 284.7 eV were used as a calibration for all binding energies.

3.5. Photocatalytic Experiment and Setup

The photo experiments were carried out in a commercial 250 mL (however maximum capacity is ~320 mL) Ace Glass Photochem reactor body equipped with two inlets (one is the gas inlet and another one is for the thermometer) and a gas outlet. A quartz immersion well from Ace Glass was used, equipped with a water inlet and outlet, to keep the medium pressure quartz mercury-vapor lamp (450 W; spectral distribution: ~40–48% is in the UV portion, 40–43% in the visible, and the balance in the IR region). The experimental temperature was maintained at ~50 °C for the whole time by the circulation of cold water in the outer jacket of the immersion well. The Photochem reactor was filled with 300 mL of distilled water with 0.3 g from each photocatalytic material after sonicating for 20 min and the solution mixture was subjected to stirring using a magnetic stir bar. A calibrated gas mixture of 20% methane and balance nitrogen from Gasco Gas was bubbled (100 mL/min) continuously through the photocatalytic reactor. After bubbling the gas mixture for 30 min to reach the adsorption–desorption equilibrium, the medium pressure

Hg lamp was turned on and the headspace from the Photochem reactor was analyzed using a gas chromatograph (Shimadzu GC-2014). The first analyte of the headspace was taken after 15 min from turning on the lamp and then the next analytes were taken at 30 min intervals. Heating tape was used to prevent headspace condensate between the reactor and GC. To improve photocatalytic activity, 2.0 mM H_2O_2 was used as an oxidant.

3.6. Analytical Determination

Detection and quantification of CH_3OH were carried out using a Shimadzu GC-2014 chromatograph equipped with a capillary column (SH-Rtx Wax column), and a flame ionization detector (FID). Pure N_2 gas was used as carrier gas. A six-port valve (VICI VALCO®) with a 1.0 mL loop was connected to the circuit to allow gas sample injection into GC. The injector and detector temperatures were adjusted at 120 and 200 °C, respectively. The oven temperature for the column was initially set at 30 °C for 7 min and then the temperature was raised to 70 °C at a rate of 10 °C/min with a hold at this temperature for 2 min. Finally, the temperature was raised to 200 °C at a rate of 40 °C/min with a hold of 3 min temperature to remove water from the column. Under these conditions, a good separation of the peaks of products can be achieved and water can be effectively removed from the column. The amount of methanol in the samples was determined by comparing the peak area of methanol in the photoreaction headspace samples to that of the peak area of the methanol in self-prepared standards.

4. Conclusions and Future Directions

The photocatalytic partial oxidation of methane to methanol over a morphologically controlled WO_3 using H_2O_2 was examined. In selected structures, they have a similar surface chemical composition with W atoms at the highest oxidation state according to the XPS spectra; however, their bandgaps, surface areas, and crystal systems are different. This study revealed that the photocatalytic activity of WO_3 toward methanol production has enhanced by a factor of approximately four by the addition of 2 mM H_2O_2. However, the formation of methanol was negatively affected when the H_2O_2 concentration was doubled. The highest methanol production rates among the morphologies that were selected belong to the WO_3 flowers/2 mM H_2O_2 (38.17 ± 3.24 μmol/g-h). A 3D hierarchical structure (WO_3 flowers) greatly enhances the photocatalytic activity towards selective photo-oxidation of methane to methanol. This high photoactivity may be due to the slow recombination of charge carriers, multiple light reflections from the hollow chambers and petal-like structure leading to high light absorption, and the comparatively high surface area of WO_3 flowers. According to our findings, morphology-controlled (especially 3D hierarchical structures) WO_3 can be superior in surface area to morphology-random WO_3 as a catalyst when used for photo-oxidation of methane to methanol. Lastly, another observed trend indicates that methanol yields decayed in the over catalysis with monoclinic and orthorhombic phases (microns, wires, and flowers), but remained constant for a certain amount of time for the hexagonal phases (rods and wires). These data suggest that a surface structural difference exists, so an in-depth study of the facet dependence of WO_3 could be informative.

Supplementary Materials: The following supporting information can be downloaded at: https://www.mdpi.com/article/10.3390/methane2010008/s1, Figure S1: PXRD spectra of WO_3 morphologies; Figure S2: WO_3 Flowers with different electron scavengers (Reaction conditions; temperature = 50 °C, pH = ~7, UV light irradiation, CH4/N2 bubbling with 100 mL/min); Figure S3. The yield of methanol in the photocatalytic partial oxidation of methane for WO_3 flowers/2 mM H_2O_2 (Reaction conditions; temperature = 50 °C, pH = ~7, UV light irradiation, CH_4/N_2 bubbling with 100 mL/min); Figure S4. FESEM image of WO_3 nanowires with high agglomeration.

Author Contributions: Writing—original draft preparation, D.P.; writing—review and editing, M.D.H. All authors have read and agreed to the published version of the manuscript.

Funding: NSF Award #11A-1301346 along with support from New Mexico Tech and Rochester Institute of Technology.

Acknowledgments: Acknowledgment is made to NSF Award #11A-1301346 along with support from New Mexico Tech and Rochester Institute of Technology. Additionally, we thank Michael Mehan of the Xerox Corporation, Webster, NY for the XPS analysis of the samples.

Conflicts of Interest: The authors declare no conflict of interest.

References

1. Tian, Y.; Piao, L.; Chen, X. Research Progress on the Photocatalytic Activation of Methane to Methanol. *Green Chem.* **2021**, *23*, 3526–3541.
2. Cortie, D.; Yi, Z.; Chen, X.; Li, Y.; Pan, X.; Huang, X. Photocatalytic Oxidation of Methane over Silver Decorated Zinc Oxide Nanocatalysts. *Nat. Commun.* **2016**, *7*, 1–8.
3. Yang, J.; Hao, J.; Wei, J.; Dai, J.; Li, Y. Visible-Light-Driven Selective Oxidation of Methane to Methanol on Amorphous FeOOH Coupled m-WO_3. *Fuel* **2020**, *266*, 117104. [CrossRef]
4. Yu, Y.; Zhang, X.; Liu, J.-W.; Lee, Y.; Li, X. Natural Gas Hydrate Resources and Hydrate Technologies: A Review and Analysis of the Associated Energy and Global Warming Challenges. *Energy Environ. Sci.* **2021**, *14*, 5611–5668. [CrossRef]
5. Hashiguchi, B.G.; Hövelmann, C.H.; Bischof, S.M.; Lokare, K.S.; Leung, C.H.; Periana, R.A. *Methane-to-Methanol Conversion. Energy Production and Storage: Inorganic Chemical Strategies for a Warming World*; Wiley: Hoboken, NJ, USA, 2010; pp. 101–142.
6. Arminio-Ravelo, J.A.; Escudero-Escribano, M. Strategies toward the Sustainable Electrochemical Oxidation of Methane to Methanol. *Curr. Opin. Green Sustain. Chem.* **2021**, *30*, 100489. [CrossRef]
7. de Klerk, A. Engineering Evaluation of Direct Methane to Methanol Conversion. *Energy Sci. Eng.* **2015**, *3*, 60–70. [CrossRef]
8. Hao, J.; Schwach, P.; Fang, G.; Guo, X.; Zhang, H.; Shen, H.; Huang, X.; Eggart, D.; Pan, X.; Bao, X. Enhanced Methane Conversion to Olefins and Aromatics by H-Donor Molecules under Nonoxidative Condition. *ACS Catal.* **2019**, *9*, 9045–9050. [CrossRef]
9. Cai, X.; Fang, S.; Hu, Y.H. Unprecedentedly High Efficiency for Photocatalytic Conversion of Methane to Methanol over Au–Pd/TiO_2–What Is the Role of Each Component in the System? *J. Mater. Chem. A* **2021**, *9*, 10796–10802. [CrossRef]
10. Olah, G.A. Beyond Oil and Gas: The Methanol Economy. *Angew. Chemie Int. Ed.* **2005**, *44*, 2636–2639. [CrossRef]
11. Negishi, Y.; Watanabe, S.; Aoki, M.; Hossain, S.; Kurashige, W. Toward the Creation of Highly Active Photocatalysts That Convert Methane into Methanol. In *Concepts of Semiconductor Photocatalysis*; IntechOpen: London, UK, 2019; pp. 85–97.
12. Liu, Y.; Wang, L.; Xiao, F.-S. Selective Oxidation of Methane into Methanol Under Mild Conditions. *Chem. Res. Chinese Univ.* **2022**, *38*, 671–676. [CrossRef]
13. Song, H.; Meng, X.; Wang, S.; Zhou, W.; Song, S.; Kako, T.; Ye, J. Selective Photo-Oxidation of Methane to Methanol with Oxygen over Dual-Cocatalyst-Modified Titanium Dioxide. *ACS Catal.* **2020**, *10*, 14318–14326. [CrossRef]
14. Gondal, M.A.; Hameed, A.; Yamani, Z.H.; Arfaj, A. Photocatalytic Transformation of Methane into Methanol under UV Laser Irradiation over WO_3, TiO_2 and NiO Catalysts. *Chem. Phys. Lett.* **2004**, *392*, 372–377. [CrossRef]
15. Villa, K.; Murcia-López, S.; Andreu, T.; Morante, J.R. Mesoporous WO_3 Photocatalyst for the Partial Oxidation of Methane to Methanol Using Electron Scavengers. *Appl. Catal. B Environ.* **2015**, *163*, 150–155. [CrossRef]
16. Villa, K.; Murcia-López, S.; Morante, J.R.; Andreu, T. An Insight on the Role of La in Mesoporous WO_3 for the Photocatalytic Conversion of Methane into Methanol. *Appl. Catal. B Environ.* **2016**, *187*, 30–36. [CrossRef]
17. Hameed, A.; Ismail, I.M.I.; Aslam, M.; Gondal, M.A. Photocatalytic Conversion of Methane into Methanol: Performance of Silver Impregnated WO_3. *Appl. Catal. A Gen.* **2014**, *470*, 327–335. [CrossRef]
18. Noceti, R.P.; Taylor, C.E.; D'Este, J.R. Photocatalytic Conversion of Methane. *Catal. Today* **1997**, *33*, 199–204. [CrossRef]
19. Gondal, M.A.; Hameed, A.; Suwaiyan, A. Photo-Catalytic Conversion of Methane into Methanol Using Visible Laser. *Appl. Catal. A Gen.* **2003**, *243*, 165–174. [CrossRef]
20. Murcia-López, S.; Villa, K.; Andreu, T.; Morante, J.R. Partial Oxidation of Methane to Methanol Using Bismuth-Based Photocatalysts. *ACS Catal.* **2014**, *4*, 3013–3019. [CrossRef]
21. Zhou, Y.; Chen, D.; Li, N.; Xu, Q.; Li, H.; He, J.; Lu, J. Pt-Co Nanoparticles Supported on Hollow Multi-Shelled CeO_2 as a Catalyst for Highly Efficient Toluene Oxidation: Morphology Control and the Role of Bimetal Synergism. *J. Colloid Interface Sci.* **2022**, *608*, 48–59. [CrossRef]
22. Khalifeh, R.; Karimi, M.; Rajabzadeh, M.; Hafizi, A.; Nogorani, F.S. Synthesis and Morphology Control of Nano $CuAl_2O_4$ Hollow Spheres and Their Application as an Efficient and Sustainable Catalyst for CO_2 Fixation. *J. CO2 Util.* **2020**, *41*, 101233. [CrossRef]
23. Dong, P.; Hou, G.; Xi, X.; Shao, R.; Dong, F. WO_3-Based Photocatalysts: Morphology Control, Activity Enhancement and Multifunctional Applications. *Environ. Sci. Nano* **2017**, *4*, 539–557. [CrossRef]
24. Pan, H.; Risley, V.A.; Martindale, K.R.; Heagy, M.D. Photocatalytic Reduction of Bicarbonate to Formic Acid Using Hierarchical ZnO Nanostructures. *ACS Sustain. Chem. Eng.* **2018**, *7*, 1210–1219. [CrossRef]
25. Murillo-Sierra, J.C.; Hernández-Ramírez, A.; Hinojosa-Reyes, L.; Guzmán-Mar, J.L. A Review on the Development of Visible Light-Responsive WO_3-Based Photocatalysts for Environmental Applications. *Chem. Eng. J. Adv.* **2021**, *5*, 100070. [CrossRef]
26. Farhadian, M.; Sangpour, P.; Hosseinzadeh, G. Morphology Dependent Photocatalytic Activity of WO_3 Nanostructures. *J. Energy Chem.* **2015**, *24*, 171–177. [CrossRef]

27. Xu, D.; Jiang, T.; Wang, D.; Chen, L.; Zhang, L.; Fu, Z.; Wang, L.; Xie, T. PH-Dependent Assembly of Tungsten Oxide Three-Dimensional Architectures and Their Application in Photocatalysis. *ACS Appl. Mater. Interfaces* **2014**, *6*, 9321–9327. [CrossRef] [PubMed]
28. Shandilya, P.; Sambyal, S.; Sharma, R.; Mandyal, P.; Fang, B. Properties, Optimized Morphologies, and Advanced Strategies for Photocatalytic Applications of WO_3 Based Photocatalysts. *J. Hazard. Mater.* **2022**, *428*, 128218. [CrossRef]
29. Pan, H.; Martindale, K.R.; Heagy, M.D. Iron Oxide Nanostructures for the Reduction of Bicarbonate to Solar Fuels. *Top. Catal.* **2018**, *61*, 601–609. [CrossRef]
30. Li, Y.; Zhang, Q.; Li, X.; Bai, H.; Li, W.; Zeng, T.; Xi, G. Ligand-Free and Size-Controlled Synthesis of Oxygen Vacancy-Rich WO_{3-x} Quantum Dots for Efficient Room-Temperature Formaldehyde Gas Sensing. *RSC Adv.* **2016**, *6*, 95747–95752. [CrossRef]
31. Jeyapaul, T.; Prakash, K.; Harikengaram, S.; Chellamani, A.; Selvam, V. Synthesis of WO_3 Nanorods and Their Photocatalytic Degradation of Organic Contaminants. *Rasayan J. Chem* **2018**, *11*, 1405–1414. [CrossRef]
32. Kong, L.; Guo, X.; Xu, J.; Mo, Z.; Li, L. Morphology Control of WO_3 Nanoplate Film on W Foil by Oxalic Acid for Photocatalytic Gaseous Acetaldehyde Degradation. *J. Photochem. Photobiol. A Chem.* **2020**, *401*, 112760. [CrossRef]
33. Acharyya, S.S.; Ghosh, S.; Bal, R. Fabrication of Three Dimensional (3D) Hierarchical Ag/WO_3 Flower-like Catalyst Materials for the Selective Oxidation of m-Xylene to Isophthalic Acid. *Chem. Commun.* **2015**, *51*, 5998–6001. [CrossRef] [PubMed]
34. Wei, S.; Xing, Y.; Li, Y.; Zhao, Y.; Du, W.; Zhou, M. Preparation and Gas Sensing Properties of Flower-like WO_3 Hierarchical Architecture. *Vacuum* **2016**, *129*, 13–19. [CrossRef]
35. Zeng, W.; Zhang, H.; Wang, Z. Effects of Different Petal Thickness on Gas Sensing Properties of Flower-like $WO_3 \cdot H_2O$ Hierarchical Architectures. *Appl. Surf. Sci.* **2015**, *347*, 73–78. [CrossRef]
36. Li, Y.; Tang, Z.; Zhang, J.; Zhang, Z. Fabrication of Vertical Orthorhombic/Hexagonal Tungsten Oxide Phase Junction with High Photocatalytic Performance. *Appl. Catal. B Environ.* **2017**, *207*, 207–217. [CrossRef]
37. Zhang, J.; Zhang, P.; Wang, T.; Gong, J. Monoclinic WO_3 Nanomultilayers with Preferentially Exposed (002) Facets for Photoelectrochemical Water Splitting. *Nano Energy* **2015**, *11*, 189–195. [CrossRef]
38. Sharon, M.; Sharan, M.K.; Jawalekar, S.R. Preparation and Characterisation of Oxygen Deficient WO_3 Film-1. *Sol. Energy Mater.* **1984**, *10*, 329–334. [CrossRef]
39. Huang, J.; Xu, X.; Gu, C.; Fu, G.; Wang, W.; Liu, J. Flower-like and Hollow Sphere-like WO_3 Porous Nanostructures: Selective Synthesis and Their Photocatalysis Property. *Mater. Res. Bull.* **2012**, *47*, 3224–3232. [CrossRef]
40. Wei, S.; Li, S.; Wei, R.; Liu, S.; Du, W. Different Morphologies of WO_3 and Their Exposed Facets-Dependent Acetone Sensing Properties. *Sens. Actuators B Chem.* **2021**, *329*, 129188. [CrossRef]
41. Weng, B.; Wu, J.; Zhang, N.; Xu, Y.-J. Observing the Role of Graphene in Boosting the Two-Electron Reduction of Oxygen in Graphene–WO_3 Nanorod Photocatalysts. *Langmuir* **2014**, *30*, 5574–5584. [CrossRef]
42. Ji, R.; Zheng, D.; Zhou, C.; Cheng, J.; Yu, J.; Li, L. Low-Temperature Preparation of Tungsten Oxide Anode Buffer Layer via Ultrasonic Spray Pyrolysis Method for Large-Area Organic Solar Cells. *Materials* **2017**, *10*, 820. [CrossRef]
43. Villa, K.; Murcia-López, S.; Andreu, T.; Morante, J.R. On the Role of WO_3 Surface Hydroxyl Groups for the Photocatalytic Partial Oxidation of Methane to Methanol. *Catal. Commun.* **2015**, *58*, 200–203. [CrossRef]
44. Wang, J.; Khoo, E.; Lee, P.S.; Ma, J. Synthesis, Assembly, and Electrochromic Properties of Uniform Crystalline WO_3 Nanorods. *J. Phys. Chem. C* **2008**, *112*, 14306–14312. [CrossRef]